

# IGNITION OF HYDROGEN-AIR MIXTURES BY MOVING HEATED PARTICLES

Melguizo-Gavilanes, J., Coronel, S., Mével, R., and Shepherd, J.E.

Explosion Dynamics Laboratory  
Graduate Aerospace Laboratories of the California Institute of Technology (GALCIT)  
Pasadena, CA, USA, josuemg@caltech.edu

## ABSTRACT

Studying thermal ignition mechanisms is a key step for evaluating many ignition hazards. In the present work, two-dimensional simulations with detailed chemistry are used to study the reaction pathways of the transient flow and ignition of a stoichiometric hydrogen-air mixture by moving hot spheres. For temperatures above the ignition threshold, ignition takes place after a short time between the front stagnation point and separation location depending upon the sphere's surface temperature. Closer to the threshold, the volume of gas adjacent to the separation region ignites homogeneously after a longer time. These results demonstrate the importance of boundary layer development and flow separation in the ignition process.

## 1. INTRODUCTION

Improved scientific understanding and characterization of ignition is of prime importance to evaluating the risk of accidental fire and explosions [1] in commercial aviation, nuclear power plants and the chemical process sector. Typical thermal ignition sources include concentrated hot surfaces, moving hot particles and extended hot surfaces [2]. The present study focuses on the ignition of stoichiometric hydrogen-air mixtures by moving heated spheres through two-dimensional numerical simulations using detailed chemistry. Special attention is given to the dynamics of the ignition process close to the minimum temperature required to induce ignition as well as at much higher temperatures.

The aim of this study is not to quantify ignition thresholds, analyze effect of particle size or material like in previous experimental and numerical work [3, 4], but to explain the dynamics of ignition when close and far from the ignition limit, and study the competition between diffusive, convective losses, and chemical heat release to ultimately unravel the complex physics and chemistry at play within the thermal boundary layer during the ignition process. Numerical tests were run with sphere surface temperatures of 900 – 1200 K to find the ignition threshold. The minimum ignition temperature for a 4 mm diameter sphere was found to be 960 K. Silver [3] found an experimental threshold of 1083 K. The 123 K difference is due to the higher particle velocity (larger convective losses) Silver used in his experiments, nearly twice as fast as in the current simulations.

## 2. PHYSICAL MODEL, NUMERICAL APPROACH AND SIMULATION PARAMETERS

### 2.1. Overview

We model the motion, transport and chemical reaction in the gas surrounding the particle by the variable-density reactive Navier-Stokes equations with temperature dependent transport properties. The surface

of the sphere is assumed to be at a fixed (uniform) temperature providing an isothermal boundary condition for the gas.

$$\frac{\partial \rho}{\partial t} + \nabla \cdot (\rho \mathbf{u}) = 0 \quad (1)$$

$$\frac{\partial(\rho \mathbf{u})}{\partial t} + \nabla \cdot (\rho \mathbf{u} \mathbf{u}) = -\nabla p + \nabla \cdot \boldsymbol{\tau} + \rho \mathbf{g} \quad (2)$$

$$\frac{\partial(\rho h)}{\partial t} + \nabla \cdot (\rho \mathbf{u} h) = \nabla \cdot (\kappa / c_p \nabla h) + q_{chem} + \frac{Dp}{Dt} \quad (3)$$

$$\frac{\partial(\rho Y_i)}{\partial t} + \nabla \cdot (\rho \mathbf{u} Y_i) = \nabla \cdot (\rho D_i \nabla Y_i) + \Omega_i \quad (4)$$

$$\text{with } p = \rho \bar{R} T, \quad \boldsymbol{\tau} = \left( p + \frac{2}{3} \mu \nabla \cdot \mathbf{u} \right) \mathbf{I} + \mu [\nabla \mathbf{u} + (\nabla \mathbf{u})^T] \quad (5)$$

The Sutherland Law, the Eucken relation and the JANAF polynomials are used to account for the functional temperature dependence of mixture viscosity ( $\mu$ ), thermal conductivity ( $\kappa$ ) and specific heat ( $c_p$ ) respectively. The chemistry is modeled using Mével's detailed mechanism for hydrogen oxidation which includes 9 species and 21 reactions [5, 6]. In equations (1)-(5),  $\rho$  is density,  $\mathbf{u}$  is the velocity vector,  $p$  is pressure,  $T$  is the gas temperature,  $h$  is the mixture enthalpy,  $\mathbf{g}$  is the gravitational acceleration,  $q_{chem} = \sum h_i \Omega_i$  is the stored chemical energy,  $Y_i$  is the mass fraction of species,  $\Omega_i = \rho dY_i/dt$  represents the rate of production/consumption of species, and  $\bar{R}$  is the specific gas constant. The Lewis number is assumed to be unity which results in  $\kappa/c_p = \rho D_i$ , hence, the dynamic thermal diffusivity of species is used to model its mass diffusivity.

The equations above are integrated in two dimensions using the Open source Field Operation And Manipulation (OpenFOAM) toolbox [7]. The spatial discretization of the solution domain is done using finite volumes, and the pressure-velocity coupling is achieved using the PIMPLE (PISO+SIMPLE) algorithm. The computational domain consists of a vertical rectangle with a 2D-axisymmetric sphere located at  $(0, 0, 0)$  with diameter  $d = 4$  mm. The top, bottom and side boundaries are placed  $15d$ ,  $5d$  and  $10d$  away from the center of the sphere respectively. A resolution of approximately 300,000 cells is used, with finer resolution near the sphere; with a minimum cell size of  $60 \mu\text{m}$  to ensure that the thermal/hydrodynamic boundary layers are properly resolved. The simulation is carried out with initial and boundary conditions that reproduce the experimental conditions used by Coronel et al. [8].

The numerical integration is divided in two parts: first, a free fall in  $\text{N}_2$  for  $0.25$  s (fall time measured experimentally) during which a steady thermal boundary layer develops. Second, contact with reactive stoichiometric hydrogen-air mixture ( $Y_{H_2} = 0.0283$ ,  $Y_{O_2} = 0.2264$ ,  $Y_{N_2} = 0.7453$ ) for 20 ms (experimental observation window) or until ignition is observed and initial stages of flame propagation take place. Initial conditions are  $p_o = 101$  kPa,  $T_o = 300$  K,  $\mathbf{u}_o = (0, 0, 0)$  m/s and a constant sphere surface temperature,  $T_{sphere}$ . Two cases are studied in detail, 960 K and 1200K. The frame of reference is attached to the sphere, hence, a time dependent inflow boundary condition is prescribed at the bottom of the computational domain to properly simulate the fall of the heated particle, as its velocity increases at a rate of  $g = 9.81$  m/s<sup>2</sup>, given by  $\mathbf{u}(t) = (0, gt, 0)$  m/s. At the top, a non-reflective/pressure transmissive boundary condition is used to simulate an outflow.

## 2.2. Comparison with Non-Reactive Experiments

In order to test the heat transfer and fluid mechanics in the numerical model, an experimental temperature field of air heated by a 6 mm diameter sphere was compared with a simulated temperature field. A slightly larger sphere was used to facilitate the postprocessing of the experimental results and to ensure enough spatial resolution in the vicinity of the sphere was achieved. Figure 1(Left) shows the temperature field and contours of constant gas temperature obtained experimentally and numerically. The

simulation predicts a smaller temperature gradient in the rear stagnation point of the sphere. In both the experiment and simulation, the thermal boundary layer grows along the curvature of the sphere. The region of flow separation is where the maximum thermal boundary layer thickness is observed. There is reasonable overall qualitative comparison between the simulation and experiment but there are clearly differences apparent in the quantitative details.

For a quantitative comparison, the temperature distribution at different axial locations (fixed values of  $y$ ) is shown in Fig 1(Right). The trends observed are very similar between the experiment and simulation in the region of interest, namely, up to the flow separation region ( $y = 2$  mm), where ignition is predicted to occur when close to the ignition threshold. For supercritical cases, ignition takes place between the front stagnation and the separation region depending upon  $T_{sphere}$ . The differences between the experiment and simulation can be attributed mostly to limitations during the postprocessing of the experimental data, specifically, the phase demodulation near boundaries (i.e. near the sphere surface), and error introduced during time averaging and calculation of the derivative in the inversion of the Abel transform and the asymmetry of the experimental flow field due to the incipient instability of the wake.

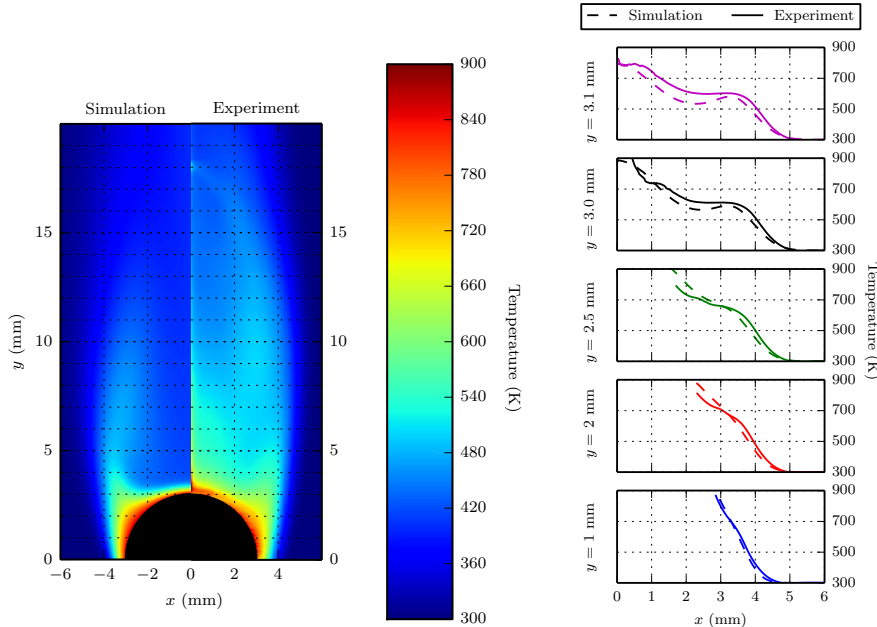


Figure 1: Left: Gas (air) temperature with contour lines of constant temperature: simulation and experiment. Right: temperature along slices of  $y$ , simulation: dashed lines; experiment: solid lines.

### 3. RESULTS AND DISCUSSION

#### 3.1. Flow structure and time to ignition

Figure 2 (Left) shows temperature and velocity (magnitude) fields obtained after  $t = 0.25$  s for  $T_{sphere} = 960$  K, together with temperature isocontours taken every 50 K from 400-950 K, and streamlines to reveal the structure of the flow. Specific locations along the sphere are uniquely determined by the angle,  $\theta$ , measured from the vertical centerline starting at the front stagnation point ( $\theta = 0^\circ$ ) and increasing towards the rear stagnation point ( $\theta = 180^\circ$ ). Development and growth of the thermal boundary layer from the front stagnation point to the region of flow separation in the vicinity of the sphere surface can be observed. There is a small temperature gradient between  $110^\circ \leq \theta \leq 130^\circ$  with temperatures as high as 900 K half a millimeter away from the sphere surface; this is in contrast with the sharp decrease from 960 K to 400 K, over the same length scale, at the front stagnation point. The edge of the hot wake of

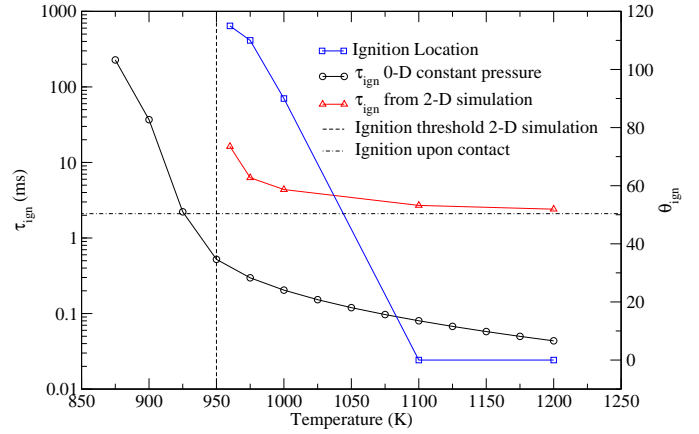
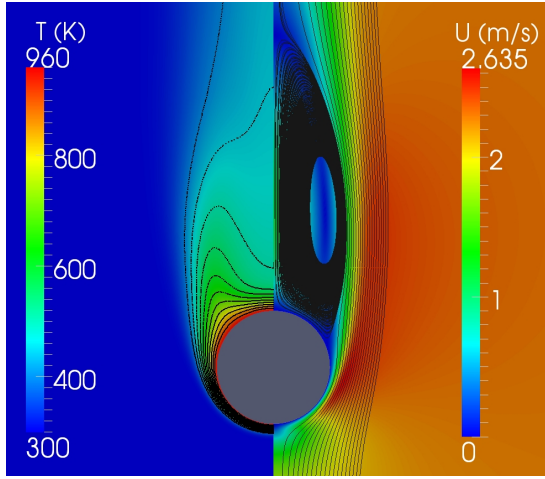


Figure 2: Left: temperature and velocity (magnitude) field in the vicinity of the sphere, temperature isocontours and streamlines. Right: comparison of ignition times obtained from 2-D simulations and constant pressure ignition times from Mével's mechanism.

the heated particle is delineated by the 400 K temperature contour. The velocity (magnitude) field and streamlines show the flow structure around the sphere. The gas is slowed as it approaches the heated particle at the front stagnation point, subsequently it is accelerated as it travels around the sphere, and finally separates at  $\theta = 115^\circ$ . The rear stagnation point, and recirculation zone can also be observed with a total length of 10 mm.

In Figure 2 (Right), the ignition times obtained from the 2-D simulations for different surface temperatures (red line) are plotted together with constant pressure delay times computed with Mével's mechanism (black line). The ignition time from the 2-D simulation increases rapidly as the temperature of the sphere is decreased to 950 K. This vertical asymptote (black dashed line) indicates the existence of a threshold, namely, the temperature below which ignition does not occur. Further examination of the curve also reveals the existence of a horizontal asymptote (black dashed-dotted line) for the temperature above which ignition takes place immediately after contact of the sphere with reactive mixture. Above 1100 K, the reaction rates are too fast for diffusive and convective losses to counteract the chemical heat release.

The blue solid line (secondary vertical axis) shows the location along the sphere where ignition occurs,  $\theta_{ign}$ , for the different surface temperatures considered. The ignition location moves from the front stagnation point ( $\theta = 0^\circ$ ) towards the zone of flow separation (near  $\theta = 115^\circ$ ) as the temperature decreases towards the minimum ignition temperature. For all the cases considered, ignition was never observed to occur in the recirculation region, hot wake, or rear stagnation point. In contrast to the 2-D simulation ignition times, the constant pressure ignition times continue to decrease as the initial temperature of the gas increases. The ratio of 2-D to 0-D ignition times for 960 K, 1000 K, 1100 K and 1200 K are 33, 25, 38 and 63 respectively. The large differences observed between the two types of simulations are due to the absence of convective and diffusive losses in the constant pressure calculations. Most importantly these large differences indicate that simplified models based on simple ignition time estimates may not be appropriate to accurately predict ignition thresholds.

In order to precisely determine the ignition time,  $\tau_{ign}$ , the temperature maximum in the computational domain is monitored during the simulation. For the present study, ignition is defined as the time at which the maximum temperature in the domain reaches  $T_{sphere} + 150$  K. Fig. 3 shows in detail the evolution of this quantity for the two sphere surface temperatures considered. The time to ignition from the initial

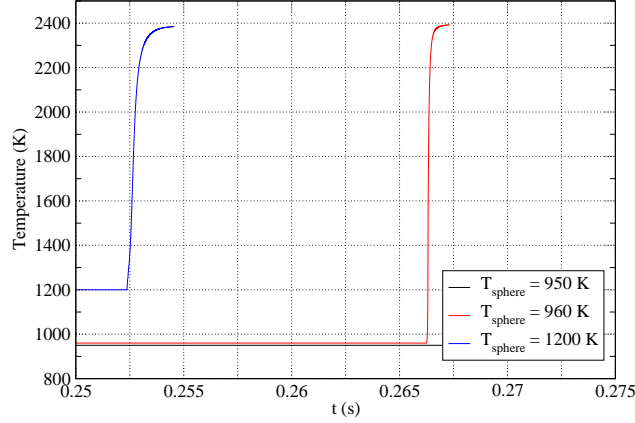


Figure 3: Temperature maximum in computational domain for  $T_{sphere} = 950, 960$  and  $1200$  K.

drop for  $T_{sphere} = 960$  K and  $1200$  K are  $\tau_{ign} = 0.266306$  s and  $0.25250$  s respectively, or alternatively, from contact with reactive mixture, the ignition times are  $16.306$  ms and  $2.5$  ms. At  $950$  K the gas does not ignite during the duration of the simulation.

### 3.2. Ignition evolution - $T_{sphere} = 1200$ K

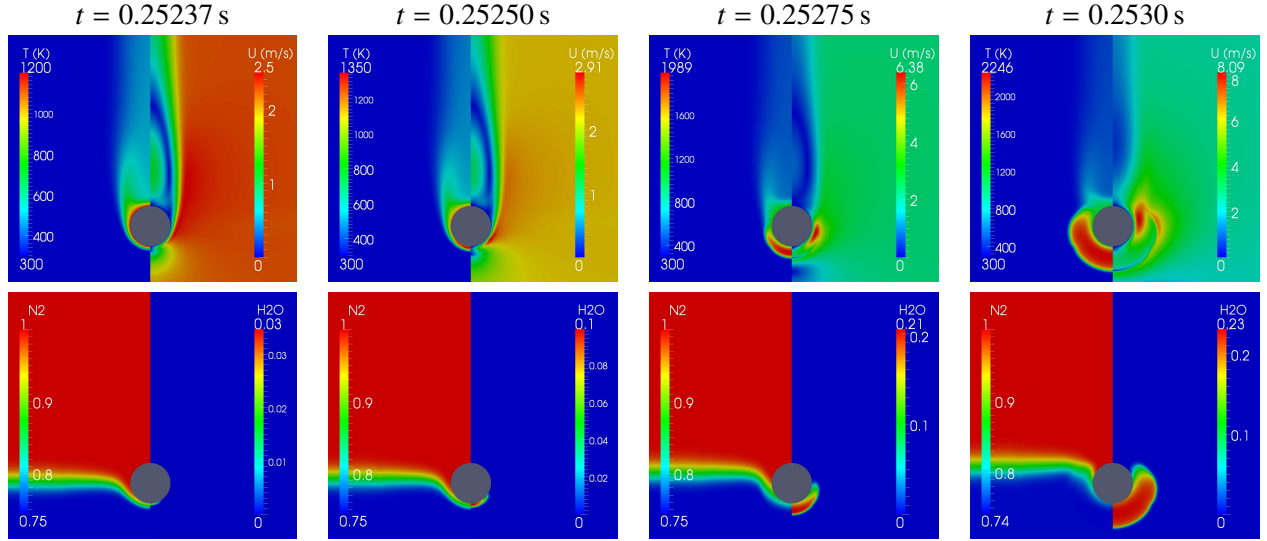


Figure 4: Ignition evolution for  $T_{sphere} = 1200$  K: temperature and velocity (magnitude) (top),  $N_2$  and  $H_2O$  (bottom) fields at  $t = 0.25237$  s - shortly before ignition,  $t = 0.25250$  s - ignition event,  $t = 0.25275$  s - shortly after ignition/flame kernel formation, and  $t = 0.2530$  s - early stages of flame propagation.

The two-dimensional fields in Fig. 4 and 5 provide additional insight into the behaviors observed. The top and bottom rows show temperature and velocity (magnitude), and  $N_2$  and product mass fraction ( $H_2O$ ) fields at four different instances during the simulation, specifically, shortly before ignition, during the ignition event, shortly after ignition/flame kernel formation and during early stages of flame propagation. The  $N_2$  mass fraction field evolution illustrate the interaction of the sphere with the inert/combustible mixture interface. The fields at  $t = 0.25237$  s exhibit the thermal and hydrodynamic boundary layer (top) as the sphere penetrates the interface (see Fig. 4 bottom row), the reactive mixture slowly pushes away the pure  $N_2$  originally present in the thermal boundary layer, which at the time scale considered here, results in  $N_2$  concentration within the boundary layer that is higher than that of

stoichiometric H<sub>2</sub>-Air. As a result, a more diluted mixture undergoes ignition. At the bottom of the figure, the section of sphere in contact with reactive mixture, the diffusion layer, and significant chemical activity (H<sub>2</sub>O=0.03) taking place upon contact at  $\theta = 0^\circ$  can be observed. During the ignition event, just 130  $\mu$ s after ( $t = 0.25250$  s), the temperature and mass fraction of products increase by 1.125 and 3.3 times to 1350 K and 0.1, from 1200 K and 0.03 respectively. Ignition occurs after 2.5 ms within the thermal boundary layer at the front stagnation point ( $\theta = 0^\circ$ ). Shortly after ignition, at  $t = 0.25275$  s, a small flame kernel forms and propagates away, preferentially over the hotter mixture present in the boundary layer (see fields at  $t = 0.25250$  s and 0.25275 s).

### 3.3. Ignition evolution - $T_{\text{sphere}} = 960$ K

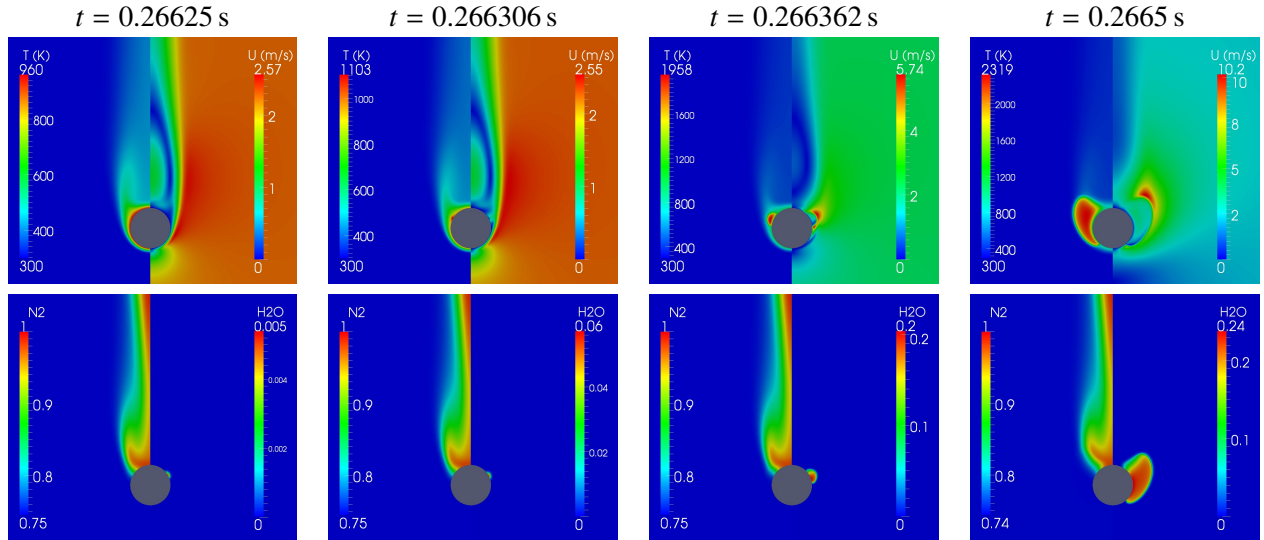


Figure 5: Ignition evolution for  $T_{\text{sphere}} = 960$  K: temperature and velocity (magnitude) (top), N<sub>2</sub> and H<sub>2</sub>O (bottom) fields at  $t = 0.26625$  s - shortly before ignition,  $t = 0.266306$  s - ignition event,  $t = 0.266362$  s - shortly after ignition/flame kernel formation, and  $t = 0.2665$  s - early stages of flame propagation.

Figure 5 shows the same fields as Fig. 4 but for a sphere surface temperature of 960 K. The temperature and product mass fraction (H<sub>2</sub>O) fields at  $t = 0.26625$  s confirm that chemical activity is localized in the region where flow separation occurs. This suggests that the reaction rates at this surface temperature are not fast enough to release sufficient heat and trigger fuel conversion into products during transit from the front stagnation point to the separation region. However, the interaction of the gas with the sphere and the flow pattern generated around it results in a separation region near  $115^\circ$  where reactive mixture is essentially trapped, conduction of heat from the sphere to the gas takes place readily, and convective losses are minimal, as confirmed by the velocity fields at  $t = 0.26625$  s. The gas in the separation region ( $\theta = 115^\circ$ ) ignites and a small flame kernel forms, as seen in the fields at  $t = 0.266306$  s and 0.266362 s respectively. At later times,  $t = 0.266362$  s, the nascent flame continues to propagate away along the circumference of the sphere, where the mixture is hottest, preferentially towards the front stagnation point and to the sides. In the rear stagnation point and recirculation zone there is no combustible mixture to be consumed, only the N<sub>2</sub> brought in by the sphere in its wake (see Fig. 5 bottom). Note also that in this case, due to the significantly longer induction time, all the N<sub>2</sub> originally present in the boundary layer has already been flushed by the H<sub>2</sub>-Air, hence, the mixture that undergoes ignition is not diluted and effectively has a higher energy content than that of the 1200 K case.

A number of differences can be emphasized regarding the early stages of flame propagation, indicated by the fields at times  $t = 0.2530$  s and  $t = 0.2665$  s for  $T_{\text{sphere}} = 1200$  K and 960 K, respectively. First, the shape of the flame is mainly determined by the extent of N<sub>2</sub> present. For instance, for the 1200 K case, the flame appears wider and has a rather shallow V-shape at the back, this is because the flame

grows and propagates only where combustible mixture is present. In this particular case, ignition occurs after 2.5 ms. The distance the sphere has traveled from the interface into H<sub>2</sub>-Air is very small in this time interval, which results in the “flatter” flame shown. On the other hand, for the 960 K case, the sphere travels almost six times as long into the combustible mixture, leaving the interface considerably further away, resulting in a narrower wake and a more pronounced V-shape at the back of the sphere. Second the flame runs away from the front stagnation point because the burning speed in stoichiometric H<sub>2</sub>-Air is higher than the speed of the falling sphere. Third, the higher temperature peak for  $T_{sphere} = 960$  K is a direct consequence of ignition occurring in an undiluted thermal boundary layer as discussed above. Fourth, the flame front pushes the gas ahead ahead of it, acting like a piston, accelerating the gas very rapidly as seen in the last two frames of the velocity fields for both cases considered.

### 3.4. Energy equation analysis

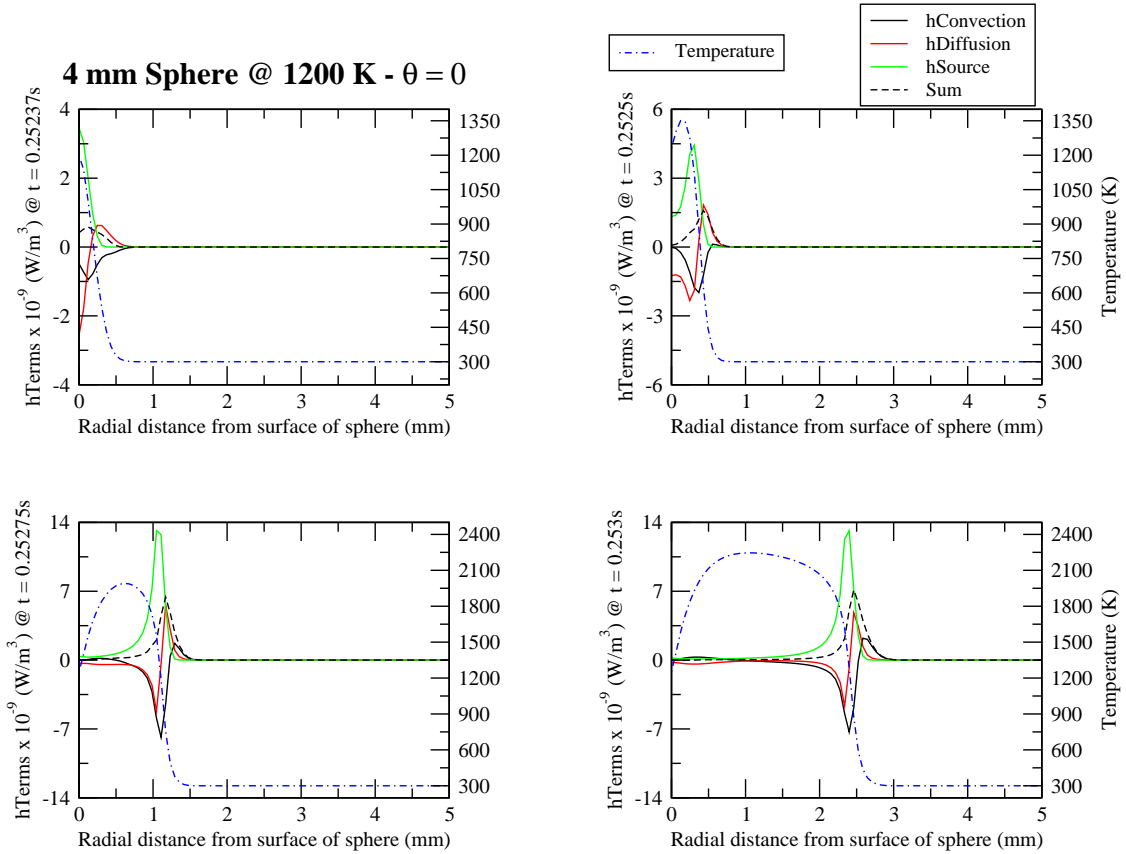


Figure 6: Ignition evolution for  $T_{sphere} = 1200$  K: contributions of each term in energy equation and temperature along radial distance from surface of sphere at  $\theta = 0^\circ$ . Top Left: at  $t = 0.25237$  s - shortly before ignition. Top Right: at  $t = 0.25250$  s - ignition event. Bottom Left: at  $t = 0.25275$  s - shortly after ignition/flame kernel formation. Bottom right: at  $t = 0.2530$  s - early stages of flame propagation.

To unravel the complex physics taking place at the ignition location,  $\theta = 0^\circ$  for  $T_{sphere} = 1200$  K and  $\theta = 115^\circ$  for  $T_{sphere} = 960$  K, each of the terms in the energy conservation equation is plotted as function of radial distance from the surface of the sphere (see Figure 6 and 7). The plots are given at the same times as the field images in Figures 4 and 5 to allow for a direct comparison. The abscissas represent the normal radial distance from the surface of the heated sphere, whereas the ordinates show the corresponding energy density and temperature. The solid lines are the convective and diffusive heat losses, and the chemical source term given respectively by  $h_{Convection} = -\nabla \cdot (\rho \mathbf{u} h)$ ,  $h_{Diffusion} = \nabla \cdot (\kappa / c_p \nabla h)$ , and  $h_{Source} = q_{chem}$ . The dashed line is the sum of the above terms, and the dashed-dotted line is the temperature. The temperature trace shows the thermal boundary layer thickness,  $\delta$ , at both

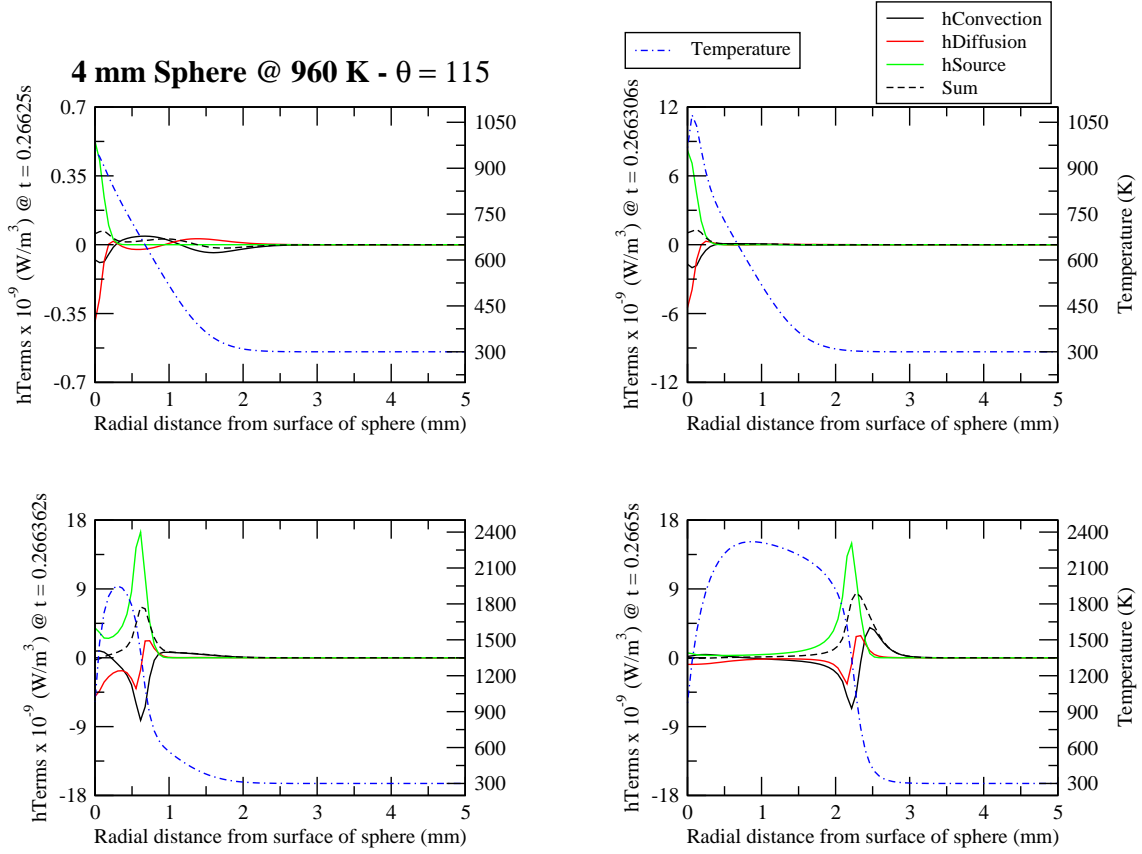


Figure 7: Ignition evolution for  $T_{sphere} = 960$  K: contributions of each term in energy equation and temperature along radial distance from surface of sphere at  $\theta = 115^\circ$ . Top Left: at  $t = 0.26625$  s - shortly before ignition. Top Right: at  $t = 0.266306$  s - ignition event. Bottom Left: at  $t = 0.266362$  s - shortly after ignition/flame kernel formation. Bottom right: at  $t = 0.2665$  s - early stages of flame propagation.

ignition locations. At  $\theta = 0^\circ$  ( $T_{sphere} = 1200$  K),  $\delta_{1200K} = 0.5$  mm, and at  $\theta = 115^\circ$  ( $T_{sphere} = 960$  K),  $\delta_{960K} = 2$  mm, this is consistent with the typical development and growth of a boundary layer on a non-reactive hot sphere.

Shortly before ignition (Figs. 6 and 7 top left), close to the sphere surface, the source term is mostly balanced by diffusion. The dip in the convective term is due to the expansion of the gas taking place in this area as a result of the initial chemical heat release; the sum is positive up to 0.5 mm normal from the sphere surface, and the temperature maximum remains at the wall. Further away from the sphere's wall (0.5 – 1 mm), convection balances diffusion (see Fig 6 top left). In Figs. 6 and 7 top right, 130  $\mu$ s and 56  $\mu$ s later, the temperature maximum is no longer at the wall but roughly 0.18 mm and 0.08 mm away from the surface of the sphere. Hence the rate at which heat is diffused back to the wall is not large enough to balance the heat released by the chemical reactions at these locations. The increase of over 17 times in the source term over 56  $\mu$ s for  $T_{sphere} = 960$  K compared with the 1.5 fold increase over a longer time interval, namely 130  $\mu$ s for  $T_{sphere} = 1200$  K further supports the idea that when close to the ignition threshold, the volume of gas confined in the separated region ignites homogeneously. The bottom left plots of Figs. 6 and 7 show the structure of an incipient flame kernel forming, with the chemical source term being balanced mostly by diffusion at the wall, and the structure of a laminar flame emerging 1 mm and 0.6 mm from the surface of the sphere, for 1200 K and 960 K respectively. The lower peak in the heat release for  $T_{sphere} = 1200$  K, namely  $13 \times 10^9$  W/m<sup>3</sup>, is, as previously mentioned, due to a more diluted mixture within the thermal boundary layer when the sphere surface temperature is far away from

the ignition threshold, and ignition times are shorter. The plots at the bottom right of Figs. 6 and 7 very clearly display the flame structure. The flame thickness can be easily estimated from the figures, it is roughly  $\sim 0.5$  mm for both cases. As the flame propagates and consumes the reactive mixture, it acts like a piston pushing the gas ahead of it which results in the convection term rapidly increasing to an absolute maximum. The subsequent drop in this term represents the expansion of the gas behind the front. Within the flame, the source term peaks abruptly at the inflection point of the temperature trace signaling the ignition of fresh mixture, it is counteracted by the combined effect of diffusion and convection.

### 3.5. Chemical Pathways

Species profiles are studied in detail and a reaction pathway analysis is performed to explain the difference in the behaviors observed when far from and at the ignition threshold. These analyses have been carried out at the ignition location obtained from the 2-D simulations. Figures 8 and 9 show the profiles of each term in the energy equation, temperature and species mass fraction for a sphere temperature of 1200 K and 960 K, respectively. In both cases, as the chemical source term overcomes the convection and diffusion terms, a sharp increase in temperature is observed along with fast consumption of the reactants and rapid production of the combustion product,  $\text{H}_2\text{O}$ , and of very reactive transient species, H, O and OH.

At  $T_{sphere} = 960$  K, the temperature drops after ignition indicating heat conduction from hot combustion products towards the sphere surface. At  $T_{sphere} = 1200$  K however, the temperature continues to increase to that of burnt products because the ignition location is further away than for 960 K and heat conduction is not significant in the time frame considered. The major species profiles show fresh combustible mixture penetrating the thermal boundary layer, slowly flushing out slowly the  $\text{N}_2$  as shown by the increase of mass fractions of  $\text{H}_2$  and  $\text{O}_2$ , and decrease of  $\text{N}_2$  starting at  $t = 0.2515$  s. Hence the mixture that undergoes ignition is significantly diluted. In the minor species profiles at 960 K there is a local maximum in the mass fraction of  $\text{H}_2\text{O}_2$  before ignition, this is in contrast with the evolution of this species at 1200 K where it peaks only after ignition takes place. Before ignition, a significant build-up of  $\text{HO}_2$  radicals is observed. This feature is more pronounced in the 960 K case.

The reaction pathway analysis is summarized in Figure 10. The main difference between the two ignition cases lies in the formation and consumption pathways of the reactive radicals H, O and OH. At high temperatures,  $T_{sphere} = 1200$  K, the hydroxyl radical is mostly (77 %) formed by the two chain branching reactions  $\text{R}_1: \text{H} + \text{O}_2 = \text{OH} + \text{O}$  and  $\text{R}_2: \text{O} + \text{H}_2 = \text{OH} + \text{H}$ . The rest is produced by the reaction  $\text{R}_3: \text{HO}_2 + \text{H} = \text{OH} + \text{OH}$ . The O atom is formed and consumed via  $\text{R}_1$  and  $\text{R}_2$ . For the H atoms  $\text{R}_4: \text{H}_2 + \text{OH} = \text{H}_2\text{O} + \text{H}$ , is the main formation path and  $\text{R}_1$  the main consumption path. At low temperature,  $T_{sphere} = 960$  K, the formation of OH (38 %) is due to the following sequence:  $\text{R}_5: \text{H} + \text{O}_2(+\text{M}) = \text{HO}_2(+\text{M})$ ;  $\text{R}_3: \text{HO}_2 + \text{H} = \text{OH} + \text{OH}$ . The chain branching reactions contribute 42 % of the OH and  $\text{R}_6: \text{H} + \text{O}(+\text{M}) = \text{OH}(+\text{M})$  amounts to 16 %. The importance of the chain branching process in the formation and consumption of the O atom and the consumption of H atom also decreases at  $T_{sphere} = 960$  K compared to 1200 K. It can be concluded that the ignition close to the threshold is delayed due to the enhanced competition between fast and direct formation of active centers via chain branching reactions and slower and indirect pathways involving linear chain processes.

## 4. CONCLUSION

Two-dimensional simulations were performed of the transient viscous flow and ignition of a stoichiometric hydrogen-air mixture by a moving hot sphere, as it penetrates through an interface between an inert ( $\text{N}_2$ ) and reactive ( $\text{H}_2$ -air) mixture. Two distinct ignition behaviors were observed. For temperatures far above the ignition threshold, reaction starts upon contact with the reactive mixture, and ignition

#### 4 mm Sphere @ 1200 K - $\theta = 0$ @ 0.36 $\delta$

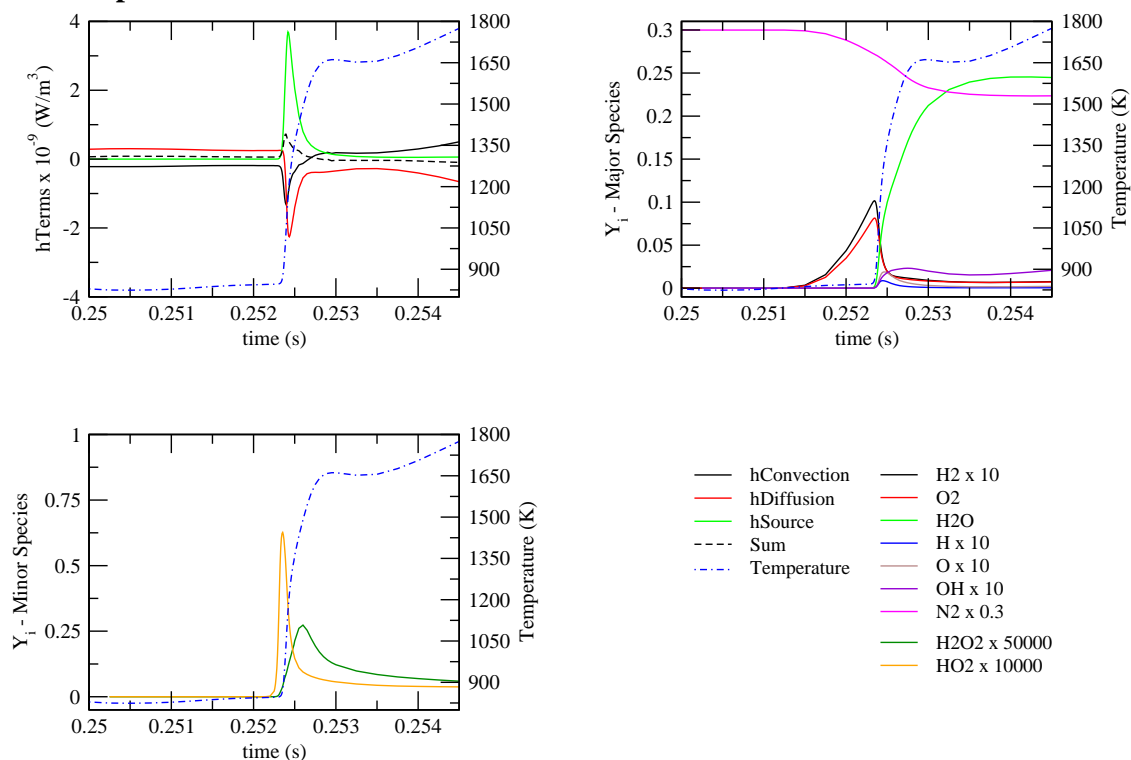


Figure 8: Temporal evolution of each term in the energy equation, temperature and species mass fractions at the ignition location for  $T_{sphere} = 1200$  K.

occurs between the front stagnation point and separation region depending upon the sphere's surface temperature. Because the ignition time is very short, there is not enough time for the pure  $N_2$  in the thermal boundary layer to be flushed out by the fresh reactive mixture and ignition takes place in a more diluted mixture. Closer to the ignition threshold, the induction time is significantly longer, and the reaction rates are not fast enough to release sufficient heat and trigger fuel conversion into products during the transit of the gas from the front stagnation point to the separation region. However separation of the boundary layer results in a zone where reactive mixture is essentially trapped, conduction of heat from the sphere to the gas takes place readily, and convective losses are minimal. The volume of gas in the separation region appears to ignite homogeneously. The large differences observed between the ignition times obtained from the two-dimensional and constant pressure simulations indicate that simplified models based on comparison of residence times with ignition delay time are inappropriate. Detailed multidimensional simulations are necessary to capture important features in the flow field such as boundary layer separation, and energy transport processes which play a significant role in the ignition process.

#### ACKNOWLEDGMENTS

This work was carried out in the Explosion Dynamics Laboratory of the California Institute of Technology, J. Melguizo-Gavilanes was supported by the Natural Sciences and Engineering Research Council of Canada (NSERC) Postdoctoral Fellowship Program, and S. Coronel and R. Mével by The Boeing Company through a Strategic Research and Development Relationship Agreement CT-BA-GTA-1.

#### 4 mm Sphere @ 960 K - $\theta = 115$ @ $0.04\delta$

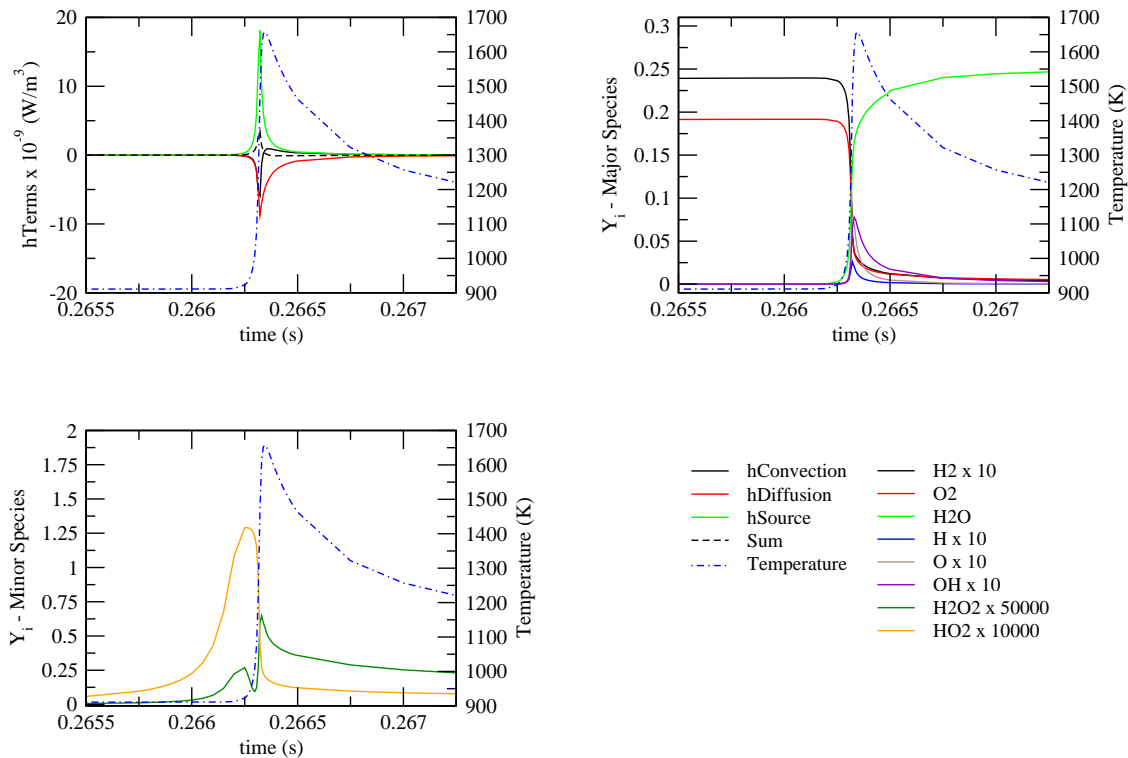


Figure 9: Temporal evolution of each term in the energy equation, temperature and species mass fractions at the ignition location for  $T_{sphere} = 960 \text{ K}$ .

## REFERENCES

1. Guidelines for determining the probability of ignition of a released flammable mass, Center for Chemical Process Safety, AIChE 2nd Edition, **2014**.
2. Brabrauskas, V., Ignition Handbook, **2003**, Fire Science Publishers.
3. Silver, R.S., The Ignition of Gaseous Mixtures by Hot Particles, *The Philosophical Magazine and Journal of Science*, **1937**, 23(156), pp. 633-657
4. Roth, D., Sharma, P., Haerber, T., Schiessl, R., Bockhorn, H. and Mass, U., Ignition by Mechanical Sparks: Ignition of Hydrogen/Air Mixtures by Submillimeter-Sized Hot Particles, *Combustion Science and Technology*, **2014**, 186(10-11), pp. 1606-1617
5. Mével, R., Javoy, S., Lafosse, F., Chaumeix, N., Dupré, G. and Paillard, C.E., Hydrogen-nitrous oxide delay time: shock tube experimental study and kinetic modelling, *Proceedings of The Combustion Institute*, **2009**, 32, pp. 359-366.
6. Mével, R., Javoy, S. and Dupré, G., A chemical kinetic study of the oxidation of silane by nitrous oxide, nitric oxide and oxygen, *Proceedings of The Combustion Institute*, **2011**, 33, pp. 485-492.
7. Weller, H.G., Tabor, G., Jasak, H., and Fureby, C., A tensorial approach to continuum mechanics using object-oriented techniques, *Journal of Computational Physics*, **1998**, 12, pp. 620-631
8. Coronel, S.A., Menon, S., Mével, R., Blanquart, G. and Shepherd, J. E., Ignition of nitrogen diluted hexane-oxygen mixtures by moving heated particles, *Proceedings of the International Colloquium on the Dynamics of Explosions and Reactive Systems*, **2013**, 24.

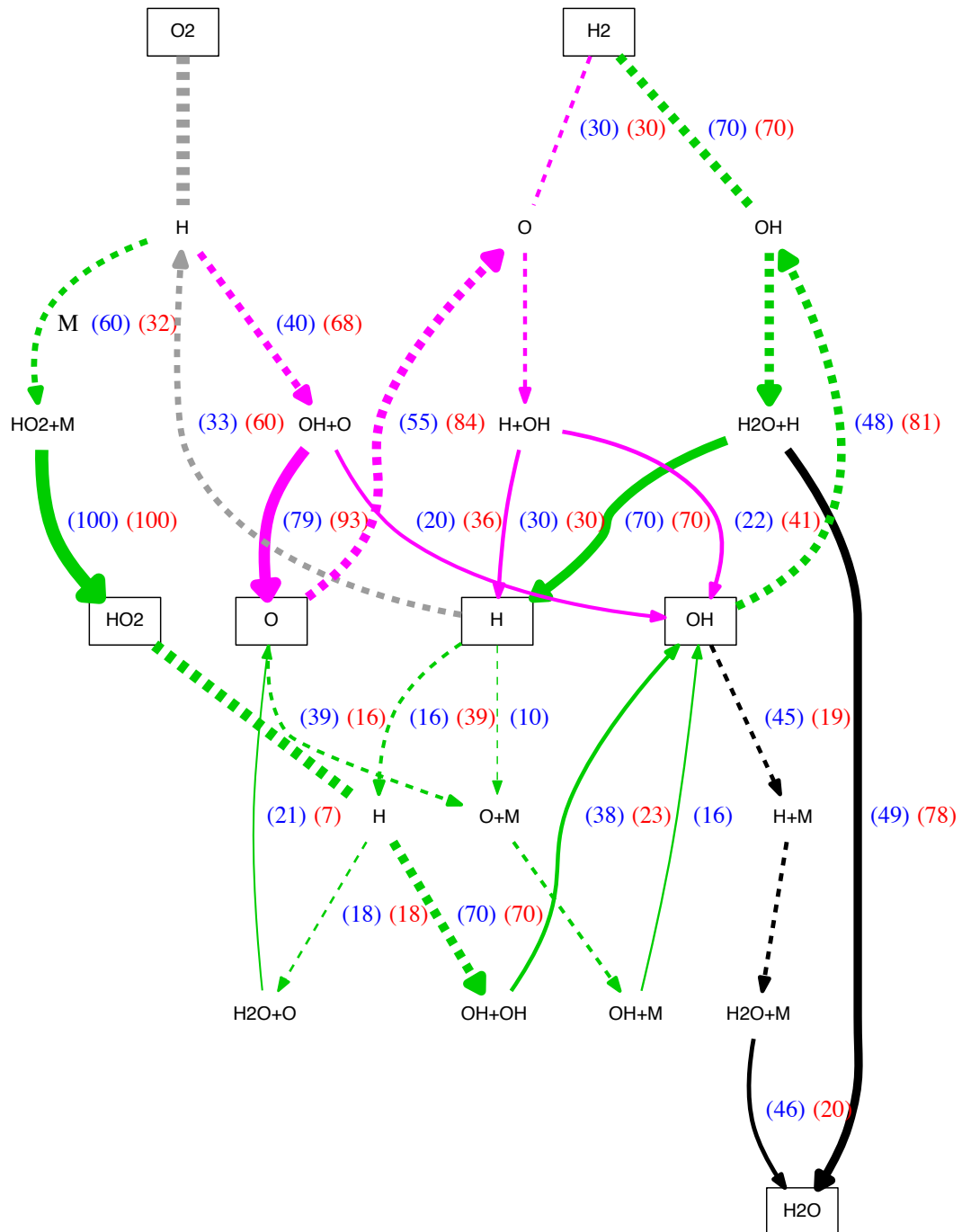


Figure 10: Reaction pathway analysis at the ignition location for  $T_{sphere} = 1200$  K (in red) and  $T_{sphere} = 960$  K (in blue). Boxes represent species reservoirs, solid lines are reservoir inputs, and dashed lines are reservoir outputs. Green: non chain branching pathways; Magenta: chain branching pathways; Grey: mixed pathways